Research
Environmental Engineering—Article

MOF-5@Ni Derived ZnO@Ni$_3$ZnC$_{0.7}$/PMS System for Organic Matter Removal: A Thorough Understanding of the Adsorption–Degradation Process

Youwen Shuai [a], Xue Huang [a], Benyin Zhang [a], Lu Xiang [a], Hao Xu [a], Qian Ye [a], Jinfeng Lu [b],*, Jing Zhang [a],*

[a] College of Architecture and Environment, Sichuan University, Chengdu 610065, China
[b] College of Environmental Science and Engineering, Nankai University, Tianjin 300071, China

ARTICLE INFO

ABSTRACT

The heterogeneous catalytic activation of peroxymonosulfate (PMS) for wastewater treatment is attracting increased research interest. Therefore, it is essential to find a sustainable, economical, and effective activated material for wastewater treatment. In this study, metal–organic framework (MOF)-5 was used as the precursor, and a stable and recyclable material ZnO@Ni$_3$ZnC$_{0.7}$ that exhibited good adsorption and catalytic properties, was obtained by the addition of nickel and subsequent calcination. To investigate and optimize the practical application conditions, the elimination of rhodamine B (RhB) in water was selected as the model process. This study demonstrated that the degradation of organic matter in the system involved a coupling of the adsorption and degradation processes. Based on this, the mechanism of the entire process was proposed. The results of scanning electron microscopy, infrared spectrum analysis, and theoretical analysis confirmed that the van der Waals forces, electrostatic attraction, and hydrogen bonding influenced the adsorption process. Electron paramagnetic resonance analysis, masking experiments, and electrochemical tests conducted during the oxidative degradation process confirmed that the degradation mechanism of RhB included both radical and non-free radical pathways, and that the surface hydroxyl group was the key active site. The degradation of the adsorbed substrates enabled the regeneration of the active sites. The material regenerated using a simple method exhibited good efficiency for the removal of organic compounds in four-cycle tests. Moreover, this material can effectively remove a variety of organic pollutants, and can be easily recovered owing to its magnetic properties. The results demonstrated that the use of heterogeneous catalytic materials with good adsorption capacity could be an economical and beneficial strategy.

© 2022 THE AUTHORS. Published by Elsevier LTD on behalf of Chinese Academy of Engineering and Higher Education Press Limited Company. This is an open access article under the CC BY-NC-ND license (http://creativecommons.org/licenses/by-nc-nd/4.0/).

1. Introduction

The progress of human society depends on the development of industry, and the latter has increasingly resulted in the production of several harmful and poisonous pollutants that are difficult to degrade in sewage. In recent years, pharmaceuticals, personal care products [1,2], and endocrine disruptors [3] that adversely affect human health and ecological environment have attracted increased research attention. Therefore, efficient methods for wastewater treatment are necessary to achieve the goal of clean production and promote the sustainable development of human society.

Several organic pollutants are difficult to remove effectively using conventional water treatment technologies [4–6], and the average removal of many organic pollutants, including atrazine, in sewage treatment plants is less than 50% [7]. To resolve this problem, advanced oxidation technologies are emerging with the rapid development of wastewater treatment technologies. Advanced oxidation processes are powerful and efficient methods to degrade the pollutants in water. Among these methods, sulphate radical-based advanced oxidation processes have attracted considerable research interest owing to their high redox potential and selectivity for oxidation [8,9]. The activation of peroxymonosulfate (PMS) can be accomplished using techniques, such as thermal activation, photoactivation [10], ultrasonic irradiation, electrochemical

methods, homogeneous metal-ion catalysis, and heterogeneous catalysis [11,12]. In recent years, heterogeneous catalysis has been widely studied owing to its high efficiency and less secondary pollution [8]. Currently, semiconductors, transition metals, and metal-free materials are widely used to activate PMS [13,14]. In addition, the development of magnetic heterogeneous catalytic materials resolves the problem of material separation in aqueous solutions and improves the possibility of practical use [15–17].

The development of heterogeneous catalytic oxidation materials encounters several problems: The use of precious metals makes the materials expensive, the catalysts are difficult to separate from the aqueous environment [18], and the recycling effect is limited [19]. In general, the development of materials is a trade-off between their cost and efficiency. Although the adsorption process is simple and economical, it does not resolve the fundamental problem of pollution in wastewater treatment. In contrast, the advanced oxidation technologies combined with the adsorption process could be more economical and efficient techniques that further promote clean and sustainable development. Several studies have investigated the application aspects of the adsorption–catalytic oxidation process. For example, Wang et al. [20] observed that the adsorption–degradation cycle was conducive to the removal of the bisphenols. Peng et al. [21] demonstrated that the synergistic effect of the adsorption and catalysis on Fe/Fe$_3$C@NG achieved an efficient removal of norfloxacin (Nor).

Metal–organic frameworks (MOFs) were selected as the potential adsorbents and heterogeneous catalytic materials owing to their large specific surface area and variable reaction sites [22,23]. MOFs are three-dimensional ordered porous materials formed by metal ions and organic ligands [24]. MOFs are also called porous coordination polymers (PCPs), and are widely used in gas storage [25], catalysis [26], adsorption [27], chemical sensing [28], drug transport [29], semiconductors [30], and biomedical imaging [31]. Moreover, many researchers have used MOFs as templates or precursors to synthesize carbonaceous materials or metal composites [32–35] to investigate their applications. MOFs-based carbon composites that are a combination of metal composites and carbon, exhibit superior potential in adsorption and heterogeneous catalysis [36,37].

However, stability is an important factor for all heterogeneous catalysts. Therefore, the practical applications of MOFs are controlled by their recycling performance and stability. Among all the reported MOFs, MOF-5 is one of the most typically used materials that exhibits open-skeleton structure, large pore surface area, and good thermal stability [38]. However, MOFs comprising divalent metal centers and multi-carboxylate ligands, such as MOF-5, are sensitive to water and can collapse in aqueous environment [39], making them less competitive in wastewater treatment. Considering that the ligands bind to nickel ions in a more stable manner than to zinc ions, the doping of MOF-5 with nickel ions can improve its stability in aqueous environment. Thus, the nickel-doped MOF-5 can be used in wastewater treatment [40]. Moreover, the addition of nickel to MOF-5 and its subsequent calcination yields a magnetic composite that facilitates the solid–liquid separation and its subsequent regeneration, as well as resolves some of the problems encountered in the development of heterogeneous materials.

We prepared a magnetic heterogeneous catalyst, denoted as ZN-CS, via a previously reported hydrothermal synthesis method [41]. The removal of rhodamine B (RhB) was selected as the model process to investigate the proposed mechanism and the coupling effects. Furthermore, the removal of different target pollutants (acid orange 7 (AO7), methylene blue (MB), tetracycline hydrochloride (TC), and Nor), and the factors affecting the degradation of RhB were studied. Finally, the analysis results of scanning electron microscopy (SEM), Brunauer–Emmett–Teller (BET) analysis, powder X-ray diffraction (XRD), Fourier transform infrared spec-

troscopy (FT-IR), and electron paramagnetic resonance (EPR) analysis and the quenching experiments demonstrated that the degradation of the absorbed pollutants enabled the regeneration of the active sites, contributing to a high recycling performance. Compared with the systems used in some previous studies, this system did not use any precious metals. Moreover, this system employed the adsorption–degradation process to achieve a balance between the economic and treatment effect. Additionally, the synthesized catalyst exhibits magnetic properties, recyclability, stable structure, and good removal efficiency for a variety of organic matter. The adsorption–interpretation coupling process provides a new approach for the development of catalytic materials with adequate adsorption performance.

2. Experiment

2.1. Materials and chemicals

Ethylene glycol, zinc nitrate hexahydrate (Zn(NO$_3$)$_2$·6H$_2$O), *N,N*-dimethylformamide (DMF), methanol, *tert*-butanol (TBA), ethanol, nickel nitrate hexahydrate (Ni(NO$_3$)$_2$·6H$_2$O), RhB, anhydrous sodium sulphate, and potassium hydrogen phosphate (K$_2$HPO$_4$) were obtained from Chengdu Kelong Chemical Reagent Co., Ltd. (China). *p*-Phthalic acid (H$_2$BDC), acid orange 7 (AO7), Oxone (PMS), and TC were obtained from Aladdin Chemistry Co., Ltd. (China). Nor and MB trihydrate were obtained from TCI (Shanghai) Development Co., Ltd. and Sinopharm Chemical Reagent Co., Ltd. (China), respectively. Ultrapure water was used to prepare all the aqueous solutions. All chemicals used in the experiments were of analytical grade.

2.2. Preparation of samples

The core–shell ZN-CS nanocomposite was prepared using a previously reported method [41] with some modifications. First, 0.75 g each of Zn(NO$_3$)$_2$·6H$_2$O and Ni(NO$_3$)$_2$·6H$_2$O were added to the solvent mixture (75 mL ethylene glycol and 120 mL DMF). The resulting sample was stirred under magnetic stirring till the solids dissolved completely. Subsequently, 0.45 g of H$_2$BDC was dissolved in the prepared solution. The solution was placed in a Teflon-lined stainless-steel autoclave at 150 °C for 6 h. The contents were collected through centrifugation, purified with ethanol and DMF, and subsequently dried in a blast drying oven at 100 °C overnight. The sample thus obtained was calcined at 450 °C in a tube furnace under a nitrogen atmosphere for 20 min, washed with deionized water. and finally dried to obtain ZnO@Ni$_3$ZnC$_{0.7}$. The high structural stability of the synthesized catalyst (denoted as ZN-CS) was confirmed using XRD and XPS analysis.

2.3. Characterization of the ZN-CS

The RhB concentration was analyzed using a spectrophotometer (MAPADA UV-1800PC, China) with maximum absorption wavelength of 554 nm. The N$_2$ adsorption/desorption isotherms were obtained using a QuadraSorb Station 2 at −196 °C. The zeta potential of the ZN-CS surface was determined using a zeta potential analyzer (Nicomp Z3000, USA). The surface morphologies and atomic composition of the newly prepared and used catalysts were analyzed using a JSM-5900LV scanning electron microscope (JEOL Ltd., Japan) equipped with an energy-dispersive X-ray spectroscopy (EDS) detector. The XRD patterns were obtained using an X'Pert Pro MPD DY129 X-ray diffractometer. Infrared spectra were obtained using FT-IR (Nicolet 6700, Thermo Scientific, USA).

2.4. Experimental operations

The adsorption performance of the ZN-CS towards RhB was studied by an extra batch-adsorption experiment in a glass beaker at 20 °C. The catalysts were withdrawn at the pre-determined intervals and immediately separated by Whatman GF/F glass-fiber membranes to measure the residual RhB concentration. To evaluate the activation ability of the ZN-CS towards PMS, catalytic experiments were conducted with the pristine ZN-CS in a 500 mL glass beaker at room temperature. Because ZnO has been widely studied as a semiconductor photocatalyst [42], we conducted a control experiment under dark conditions to eliminate the effect of light. The results thus obtained exhibited no significant difference (Appendix A Fig. S1). Therefore, the subsequent experiments were conducted under indoor light conditions. Before the addition of PMS, different dosages of the catalysts were dispersed in a 200 mL RhB solution, which was stirred for approximately 15 min to achieve the adsorption equilibrium. The degradation reaction was triggered by adding the desired amount of PMS. The samples were withdrawn, and filtered at certain time intervals to determine the residual pollutant concentration. The blank test without the catalyst was conducted under the same conditions. PMS was the principal source of hydroxyl and sulphate radicals that are essential for the degradation process. Therefore, to investigate the effect of the initial PMS concentration, experiments were carried out using PMS concentrations in the range 100–400 mg·L^{-1}. The experimental results indicated a noticeable increase in the RhB removal with 200 mg·L^{-1} PMS. Therefore, the subsequent experiments were performed using the PMS concentration of 200 mg·L^{-1}. The effect of the catalyst dosage was evaluated at 25, 50, 100, and 150 mg·L^{-1}. Additionally, the effect of the initial RhB concentration was investigated.

To study the contribution of the reactive species, methanol and TBA were used as the radical scavengers. To observe the effect of the reactive sites, dipotassium phosphate was used to mask them. The used catalysts were washed with ultrapure water and dried at 100 °C overnight. The recycling experiments were carried out at $[RhB]_0$ = 3.40 mg·L^{-1}, which was equal to the concentration of RhB after adsorption by the pristine ZN-CS at $[RhB]_0$ = 7.60 mg·L^{-1}; all other steps remained the same. All the experiments were carried out twice or thrice, and the average data with their standard deviations were presented.

3. Results and discussion

3.1. Adsorption and catalytic oxidation performance

The ZN-CS exhibited a strong adsorption affinity for RhB before the addition of PMS, with over 50% removal of RhB in 15 min (Fig. 1). The pH change of the solution during the removal process and all the kinetic results are shown in Appendix A Fig. S2, Text S1, and Table S1 separately. Additionally, the adsorption rate of RhB increased gradually, probably owing to both the decreasing RhB concentration in the aqueous phase and the gradual exhaustion of the adsorption sites. PMS was added to the solution to initiate the reaction when the adsorption equilibrium was reached. After 30 min, approximately 90% RhB was eliminated in the ZN-CS/PMS system, while only 8% RhB was removed in the PMS system. Moreover, the ZN-CS exhibited the best removal efficiency among the precursor and the catalyst with single metal (Appendix A Fig. S3). Additionally, the PMS concentration decreased rapidly in the beginning, and the decrease became gradual with time (Appendix A Fig. S4). The rapid consumption of PMS at the beginning was probably owing to the adsorption or some binding effects with the catalyst. Subsequently, the activation of PMS became
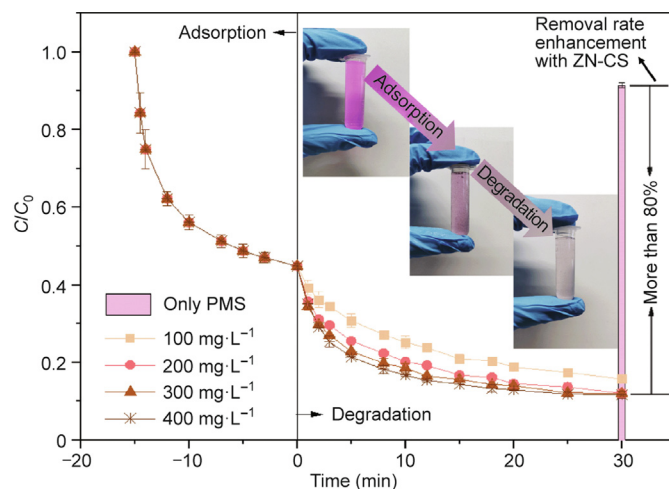

Fig. 1. Effect of the initial PMS concentration on RhB adsorption and degradation by the ZN-CS/PMS system, and RhB removal efficiency in the PMS system. Reaction conditions: [ZN-CS] = 100.00 mg·L^{-1}, $[RhB]_0$ = 7.60 mg·L^{-1}. C_0: initial RhB concentration; C: RhB concentration.

gradual because of the saturation and depletion of the active sites. Thus, the material can adsorb RhB, and activate PMS for further degradation of the substrate. The coupling effect of adsorption–degradation presents certain practical application potential (Appendix A Fig. S5). In the following analysis, the elimination process of RhB could be separated into two stages, adsorption and degradation. The possible mechanisms of both the stages were proposed.

3.2. Preliminary analysis of the catalyst composition

To confirm the crystallographic structure, phase purity, and structural stability of the ZN-CS, XRD patterns of the pristine and used samples were recorded (Fig. 2(a)). The results demonstrated that the catalyst comprised ZnO (Joint Committee on Powder Diffraction File (JCPDF) #89-0510) and Ni$_3$ZnC$_{0.7}$ (JCPDF #28-0713). The distributions of ZnO and Ni$_3$ZnC$_{0.7}$ in the shell and core were approximately uniform (Appendix A Fig. S6 and Table S2). This indicated that the sample was of high purity, and no other crystalline impurities were detected. Additionally, the phase of the used sample was confirmed by XRD analysis. The phase of the obtained catalyst remained unchanged during the process. As can be confirmed from the wide X-ray photoelectron spectroscopy (XPS) spectrum (Fig. 2(b)), the ZN-CS comprised four elements—Zn, Ni, C, and O. This result was consistent with those obtained from XRD analysis. The high-resolution Zn 2p spectrum (Fig. 2(c)) revealed two components: ZnO with binding energies of 1024.3 and 1047.6 eV, as well as Zn–Ni with two peaks positioned at 1021.7 and 1043.5 eV. The high-resolution Ni 2p spectrum (Fig. 2(d)) revealed two components: Ni(0) at 852.3 and 869.5 eV, and Ni^{2+} at 854.8 and 872.2 eV. Two shake-up satellite peaks at 859.6 and 879.1 eV were also observed. In general, the two forms of metals corresponded to the two main components—ZnO and Ni$_3$ZnC$_{0.7}$—in the XRD analysis. The formation of Ni^{2+} occurred possibly because of the surface oxidation of Ni. In addition, the relative content of ZnO slightly increased from 20% to 30% after the degradation process, indicating that Zn was partially oxidised and thus acted as an electron donor. There was no remarkable change in the valence ratio of Ni. This indicated that the contribution of metal gain and loss electrons to degradation was not significant.
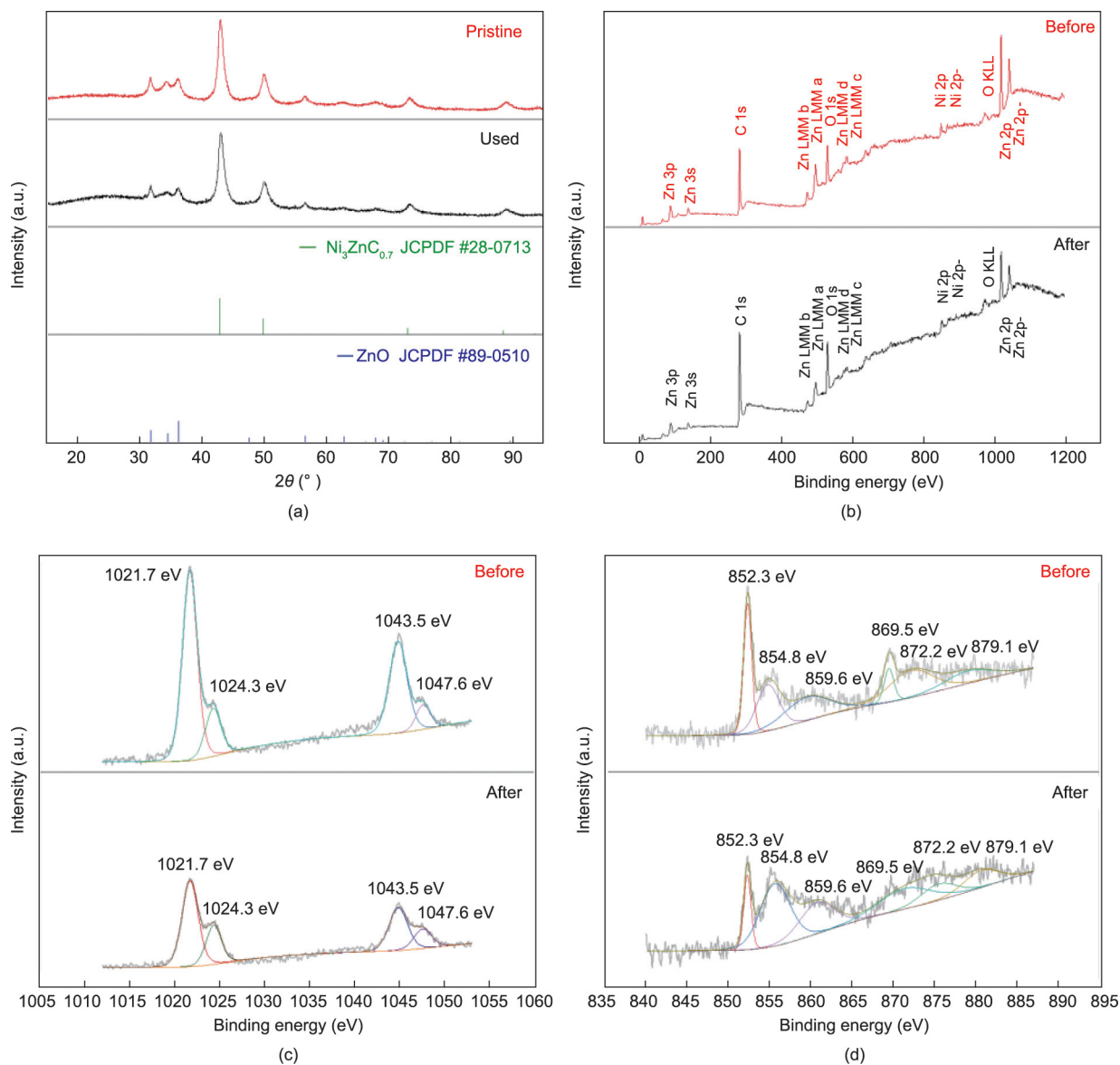
Fig. 2. (a) XRD patterns of the pristine catalyst and used catalyst, (b) wide XPS spectrum of the ZN-CS before/after degradation, (c) the high-resolution Zn 2p spectrum of the ZN-CS before/after degradation, and (d) the high-resolution Ni 2p spectrum of the ZN-CS before/after degradation.

3.3. Adsorption mechanisms

There are some classical explanations for the adsorption mechanism, including physical and chemical adsorption. Physical adsorption mainly involves the van der Waals forces and electrostatic attraction. In contrast, chemical adsorption involves the formation of chemical bonds, either by transfer or sharing of electrons, between the adsorbent molecules and the atoms or molecules on the solid surface of absorbent [43–45]. To determine the adsorption mechanisms, several experiments and theoretical calculations were conducted.

3.3.1. Physical adsorption
(1) **Physical adsorption capacity**. To determine the physical adsorption capacity of the samples, we examined their surface morphologies and atomic composition using SEM-EDS, and calculated their specific surface area and the average pore diameter by the nitrogen adsorption/desorption experiment. The synthesized catalyst exhibited a sphere-like morphology with a core–shell

structure. Fig. 3(a) presents an image of the pristine catalyst. The catalyst surface was loose and porous, with the external shape similar to that of *Hydrangea macrophylla*. Fig. 3(b) illustrates the electron micrograph of the catalyst magnified to 2000 times. The particle size of the catalyst was uniform, and the shell structures of few particles were damaged. Agglomeration in the range of approximately 2–4 μm within the particles was observed. After the adsorption, the pore channels were filled, with further aggregation of the particles (Figs. 3(c) and (d)). The catalyst shape did not change remarkably, and the core–shell structure remained stable (Figs. 3(e) and (f)) after the degradation. This was consistent with the results of XRD analysis. Owing to the continuous deposition of the surface materials, the surface pores were filled, and the particle surface was gradually passivated. This can be expected to result in a decrease in the adsorption capacity. with subsequent release of the active sites in the degradation process. Thus, the adsorption ability was regenerated for reuse. The bars in Figs. 3(d) and (f) were considered to be the impurities introduced in the recycling process. Additionally, the results of EDS analysis
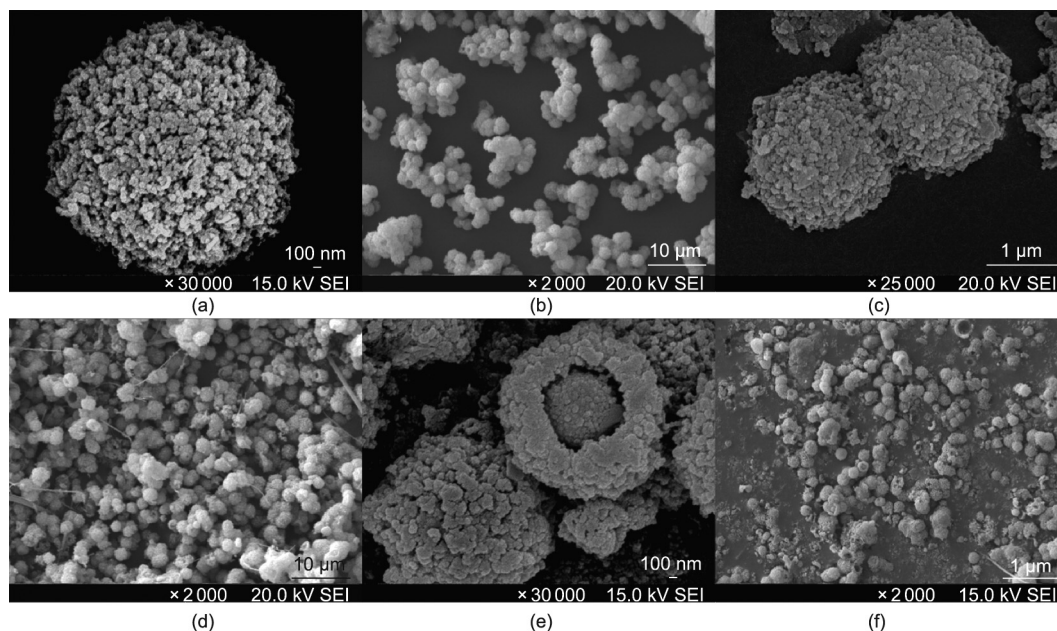
Fig. 3. SEM images of (a, b) the pristine catalyst, (c, d) catalysts after adsorption of RhB, and (e, f) catalysts after degradation of RhB.

Table 1
Changes in the surface element content of C, O, Ni, and Zn per the EDS analysis.

Catalyst	C (%)	O (%)	Ni (%)	Zn (%)
Pristine	67.37	11.81	12.22	8.60
Absorbed	69.23	12.34	11.76	6.67
Degraded	72.85	10.41	10.38	6.36

(Table 1) indicated changes in the oxygen-containing functional groups, which will be explained in the collaborative analysis of the FT-IR characterization later.

As illustrated in Fig. 4, the N_2 adsorption–desorption isotherms were identified as type II with a type H3 hysteresis loop [46]. This was owing to the presence of large pores formed by the accumulation of flaky particles, and was consistent with the morphology of
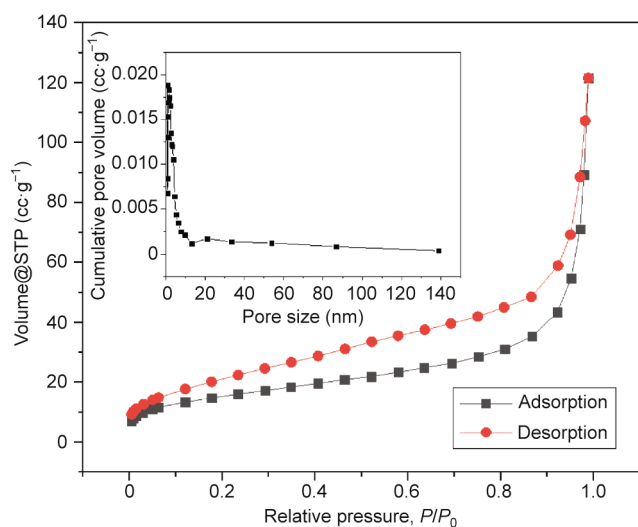

Fig. 4. N_2 adsorption–desorption isotherms and the pore-size distribution curve of the ZN-CS. STP: standard temperature and pressure; cc: cubic centimeter (cm^3); P: the nitrogen partial pressure; P_0: saturated vapor pressure of nitrogen at adsorption temperature.

the precursors. The specific surface area of the sample calculated using BET analysis was 55.311 $m^2·g^{-1}$. As can be observed from the pore-size distribution diagram, the average pore diameter of the ZN-CS was less than 20 nm. The large specific surface area and narrow pores may also contribute to the enrichment of RhB and potentially provide enough active sites for the heterogeneous reaction process.

(2) **Electrostatic attraction**. The electrostatic factor may also play an important role in the adsorption process [47] as discussed here. We measured the zeta potential of the catalyst to determine its charge properties at different pH levels. The pH value at the point of zero charge (pH_{PZC}) of the catalyst in the reaction system measured by zeta potential analyzer was approximately 7.5 (Appendix A Fig. S7). This result could be discussed from the following two aspects. First, the catalyst surface was negatively charged, and the negative charge increased with the pH value at pH > 7.5 for the ZN-CS. Moreover, when the pH was less than 7.5, the surface became positively charged, and the positive charge increased as the pH value decreased. The pK_a of RhB is 3.0 and its K_{OW} is 190 [48]. For pH > 7.5, 90% of the carboxylic acid molecules on RhB dissociated, and the number of the amphoteric ions (those containing the carboxylate ion and quaternary ammonium cation) of RhB increased with the pH value. For pH < 7.5, the carboxylic acid dissociation of RhB decreased with decrease in the pH value.

Thus, an increase in the pH value was conducive to the improvement in the electrostatic attraction between the catalyst and quaternary ammonium cation of RhB. In addition, the electrostatic repulsion between the catalyst and carboxylate ion on RhB increased with the increase in the pH value. As can be observed from Appendix A Fig. S8, an improved adsorption ability was obtained with the pH value of 3.02 or 8.96, both at severe conditions. The possible reason is that the greater charge on the catalyst

led to stronger electrostatic attractions under the abovementioned conditions.

3.3.2. The surface complexation between RhB and the ZN-CS

In addition to the physical adsorption between RhB and the ZN-CS, the surface complexation that involved chemical bonding and contributed to the adsorption process is also discussed here. As the functional groups played a vital role in the chemical bonding between the absorbent and adsorbate, FT-IR analysis of the catalyst was conducted to determine the main functional groups involved in the adsorption process. The samples were dried at 100 °C overnight to decrease the interference of the bound water with the absorption peak. The band at 750 cm^{-1} was assigned to the bending vibration of O–H (γ O–H) (Fig. 5). The broad band observed at approximately 3425 cm^{-1} was attributed to the stretching mode of O–H (ν O–H) owing to the presence of hydroxyl [18], and the decline in the band intensity might be attributed to the consumption and regeneration of the surface hydroxyl groups. Furthermore, when the catalyst was used to adsorb RhB, the abovementioned peak underwent a blue-shift of 5 cm^{-1} (from 3425 to 3430 cm^{-1}), which indicated that RhB bonded with the catalyst by replacing the O–H groups on the surface of the oxide [49,50]. Additionally, because of the vibration of the aromatic rings [51,52], a new peak at 1178 cm^{-1} was observed for the RhB-adsorbed sample. These results indicated that the adsorption mechanism involved the surface complexation between RhB and the ZN-CS. To substantiate the role of chemical adsorption, we used phosphate to mask the hydroxyl groups on the surface of the ZN-CS, as phosphate exhibits stronger affinity for this adsorption site [53]. The results revealed that the adsorption capacity decreased by approximately 10% in presence of the masking agent (Appendix A Fig. S9). This indicated that the hydroxyl groups were involved in the chemisorption.

3.3.3. Kinetic analysis

The study of adsorption kinetics is essential to elucidate the adsorption mechanism. Therefore, we calculated the kinetic data of the adsorption process using pseudo-first-order [54] and pseudo-second-order [55,56] simulations (Appendix A Text S2). The calculated kinetic data (Table 2) revealed that the adsorption process was better described with the second-order kinetics, indicating that the chemisorption was the rate-determining step [56].
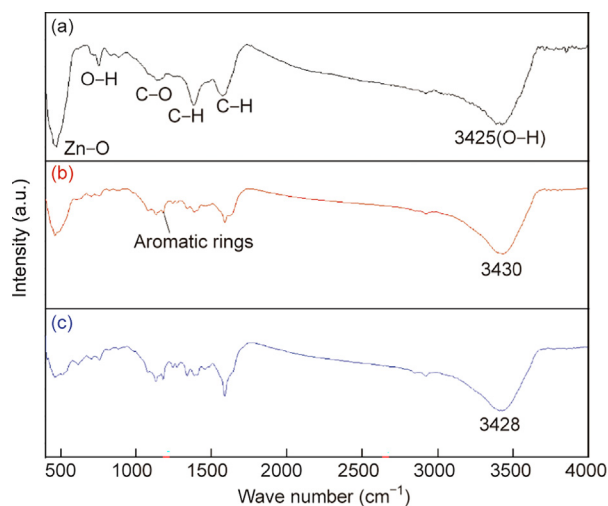

Fig. 5. FT-IR spectra of the (a) pristine catalyst, (b) catalyst after the adsorption, and (c) catalyst after the degradation.

In addition, the fitting results of different adsorption models demonstrated that the adsorption process can be best described with the Freundlich model and the sorption of RhB on the ZN-CS surface was essentially chemical (Appendix A Text S3 and Table S3). The values of thermodynamic parameters (ΔG, ΔS, and ΔH) revealed that the adsorption of RhB on the ZN-CS surface was spontaneous, feasible, and exothermic (Appendix A Fig. S10, Text S4 and Table S4). In conclusion, the adsorption process was mainly determined by the van der Waals forces, electrostatic attraction, and the surface complexation of the hydroxyl groups, with chemisorption being the rate-determining step.

3.4. The degradation mechanism

3.4.1. Identification of the active species and active sites

To determine the reactive species involved, different quenchers were used, and their contribution to the RhB degradation was investigated (Fig. 6(a)). Methanol and TBA were used to quench the $SO_4^{-\cdot}$ and $HO^{\cdot}$ radicals [57–59]. However, stronger inhibition effect was observed after the addition of TBA (Fig. 6(a)), which was contrary to what was expected. This might have resulted from the high viscosity of TBA [60]. Therefore, additional experiments were required to be conducted to identify the active species.

EPR analysis was carried out to determine the responsible radical species using dimethyl pyridine N-oxide (DMPO) and 2,2,6,6-tetramethylpiperidine (TEMP) as the spin-trap agent. The characteristic peaks corresponding to the DMPO-OH adducts and feeble signals corresponding to the DMPO-SO$_4$ adducts were observed in the PMS/ZN-CS system (Fig. 6(b)). As the capture of the trace sulphate radical in the actual detection was difficult, the signal corresponding to the DMPO-SO$_4$ adducts was weak, and had the same height as that of the noise signal. Moreover, no signal corresponding to $O_2^{-\cdot}$ was detected. These results were consistent with some previous observations [61–63]. Considering the production of the singlet oxygen during the self-decomposition of PMS [64], we conducted a controlled experiment using TEMP as the capture agent to determine if the catalyst could promote the production of the singlet oxygen. Consequently, the signal strength of the PMS system was similar to that of the PMS/ZN-CS system within the error range. This indicated that the production of the singlet oxygen cannot be facilitated in the PMS/ZN-CS system. Moreover, the self-decomposition of $SO_5^{-\cdot}$ radicals can readily proceed owing to its high reaction rate ($\approx 2 \times 10^8$ (mol·L^{-1})$^{-1}$·s^{-1}) and low activation energy (E_a = (7.4 ± 2.4) kcal·mol^{-1}), resulting in the fast generation of $^1O_2$ (Appendix A Text S5, and Eqs. (S14) and (S15)) [65–68]. Thus, it can be concluded that radicals (mainly $HO^{\cdot}$) were generated in the ZN-CS/PMS system and that these radicals played an important role in the degradation of RhB. In the radical pathway, Zn and Ni were involved in the direct redox process of PMS; the possible reaction is given in Appendix A Text S6, and Eqs. (S16)–(S19) [69–71]. However, the effect on the degradation rate was small, owing to the masking of the $SO_4^{-\cdot}$ and $HO^{\cdot}$ radicals by methanol. This suggests a more dominant mechanism of degradation.

Ding et al. [72] summarized the methods for the estimation of the contribution rates of the radical and non-radical processes (Appendix A Text S7, and Eqs. (S20)–(S22)). The results revealed that the contribution rate of the radical process was approximately 34.1%, and that of the non-radical process was approximately 65.9%. This indicates that the non-radical process played an important role in this system.

In recent years, the mechanism of the indirect oxidation of pollutants by oxidants has been proposed. Increased attention has been paid to the direct electron transfer between the pollutants and high-potential intermediates formed by the carbon materials

Table 2
Comparison between the adsorption rate constants, q_e, and the estimated and correlation coefficients (R^2) associated with the pseudo-first-order and pseudo-second-order rate equations.

Initial RhB concentration (mg·L^{-1})	Pseudo-first-order rate equation			Pseudo-second-order rate equation		
	k_1 (min^{-1})	q_e (mg·g^{-1})	R^2	k_2 (g·(mg·min)$^{-1}$)	q_e (mg·g^{-1})	R^2
3.8	0.218	4.143	0.9924	0.0098	34.602	0.9922
7.6	0.236	4.374	0.9934	0.0134	45.662	0.9984
11.4	0.183	4.756	0.9778	0.0090	52.632	0.9851
15.2	0.262	4.393	0.9895	0.0187	55.556	0.9972

k_1 (min^{-1}) and k_2 (g·(mg·min)$^{-1}$) are the adsorption rate constants of the pseudo-first-order and the pseudo-second-order models, respectively.
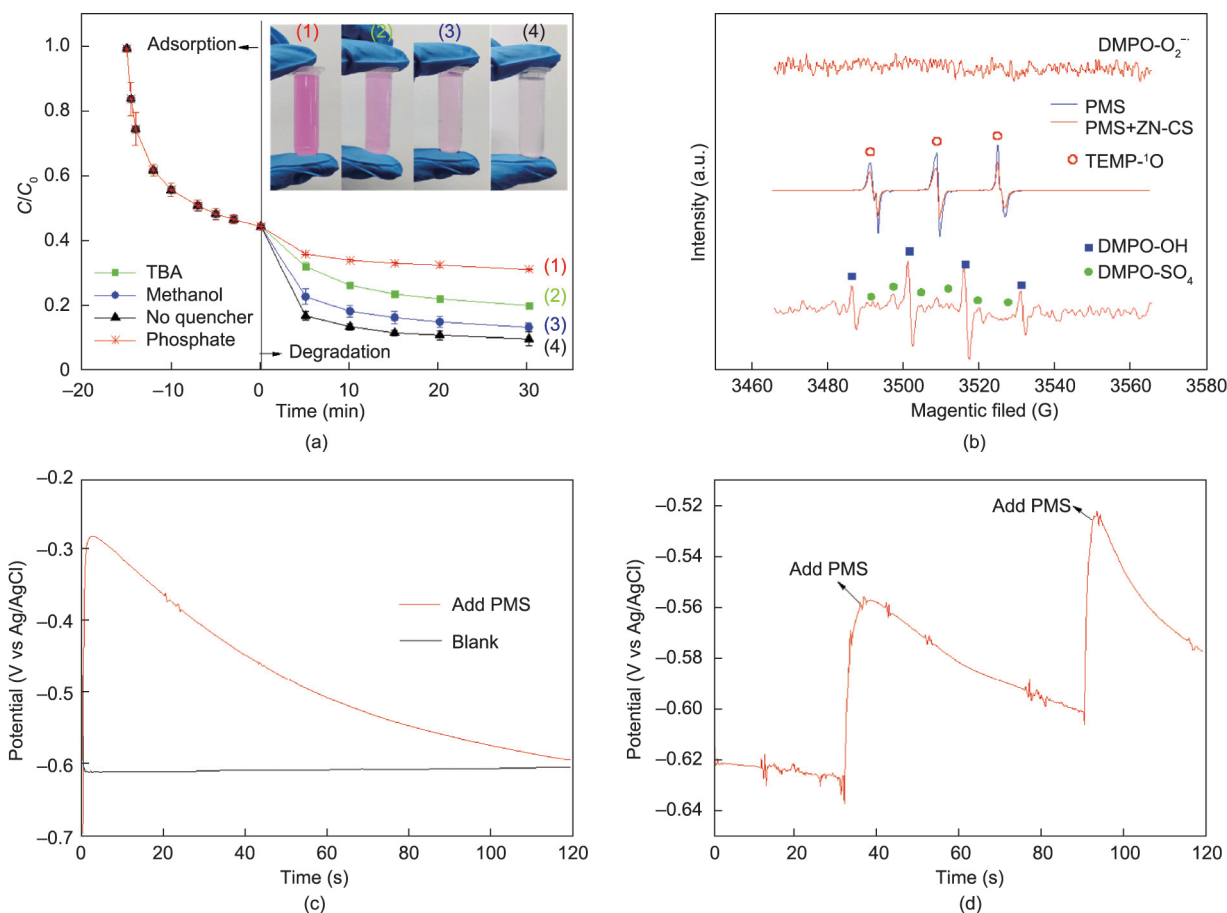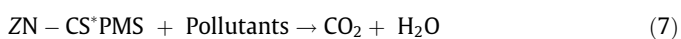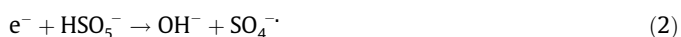

Fig. 6. (a) Effect of the quenching agents. TBA:PMS = 1000:1, methanol:PMS = 1000:1, phosphate:PMS = 5:1 (molar ratios). Reaction conditions: catalyst dose = 100.00 mg·L^{-1}, PMS dose = 200.00 mg·L^{-1}, [RhB]$_0^r$ = 7.60 mg·L^{-1}, room temperature, and pH$_0$ 6.3, (b) Dimethyl pyridine *N*-oxide (DMPO) and 2,2,6,6-tetramethylpiperidine (TEMP) spin-trapping EPR spectra of different systems; (c) the chronopotentiometry curves on the ZN-CS electrodes in different systems ([NS] = 0.5 mmol·L^{-1}, [PMS] = 200.00 mg·L^{-1}); and (d) the chronopotentiometry curves on the ZN-CS electrodes in the degradation system with gradual addition of PMS ([NS] = 0.5 mmol·L^{-1}, [RhB] = 7.60 mg·L^{-1}). NS: sodium sulphate.

and oxidants. Ren et al. [73] suggested that peroxydisulfate (PDS) can be catalyzed by carbon nanotubes (CNTs) to form a high-redox potential composite to degrade organic compounds directly. Based on his research, we used the catalyst as electrodes to confirm the formation of the high-potential intermediates (Appendix A Text S8), and monitored the open-circuit potential by chronopotentiometry analysis. The open-circuit potential increased remarkably after the addition of PMS (Fig. 6(c)), indicating that the catalyst and PMS combined to form the high-potential intermediate (denoted as ZN-CS*PMS). The gradual decrease in the potential can be attributed to the consumption of highly potential-active substances. Subsequent supplementation with PMS can aid in the recovery of the potential (Fig. 6(d)). This indicates the potential for the direct oxidation ability of ZN-CS*PMS.

Additionally, it is essential to determine the active sites on the catalysts to elucidate the mechanism. To determine the active sites that activate PMS, changes in the functional groups of the catalysts after degradation were analysed. Fig. 5 illustrates the FT-IR spectra of the ZN-CS in the range 400–4000 cm^{-1}. Six distinct adsorption bands were identified at approximately 460, 750, 1137, 1383, 1570, and 3425 cm^{-1}. As mentioned earlier, owing to the presence of the hydroxyl [18], the increased intensity of the broad band at approximately 3425 cm^{-1} indicated the regeneration of the O–H in the degradation process. The red shift of this band after the addition of PMS indicated that the complexation between RhB and the ZN-CS was destroyed, and that the RhB adsorbed on the catalyst surface was partially degraded. After the reaction, the decrease in the absorption band at approximately 460 cm^{-1} (corresponding

to the stretching of Zn–O bond) [74–77], indicated that ZnO was either consumed or leached. Finally, the remaining three spectral lines were almost the same, confirming the stability of the ZN-CS. To confirm the role of the surface hydroxyl groups, a masking experiment was conducted using a phosphate with stronger affinity [53]. The RhB degradation exhibited a remarkable inhibition (Fig. 6(a)), confirming the role of the surface hydroxyl groups in the PMS activation. ZnO is a semiconductor that contains numerous mobile electrons and exhibits good capacitance characteristics [78]. It can transfer and store electrons, and is conducive to the electron transfer and conduction between the ZN-CS*PMS intermediates and pollutants. In addition, $Ni_3ZnC_{0.7}$ exhibits good electrical conductivity [79] and electron-transfer ability. Thus, it can be assumed that Zn and Ni play an important role in the electron transfer between the ZN-CS*PMS and organic contaminants in the non-radical pathway. Therefore, Zn and Ni may act as electron donors and carriers in the free radical process, whereas in the non-radical process, both of them mainly contribute to the electron conduction. Thus, a possible degradation mechanism with the effect of organic moieties of the ZN-CS can be expressed in terms of the following equations (Eqs. (1)–(7)).

$$e^- + HSO_5^- \rightarrow SO_4^{2-} + HO^· \tag{1}$$

$$e^- + HSO_5^- \rightarrow OH^- + SO_4^{-·} \tag{2}$$

$$e^- + HSO_5^- \rightarrow SO_5^{-·} + H^+ \tag{3}$$

$$OH^- + SO_4^{-·} \rightarrow SO_4^{2-} + HO^· \tag{4}$$

$$SO_4^{2-} + HO^· \rightarrow SO_4^{-·} + OH^- \tag{5}$$

$$ZN - CS - OH + PMS \rightarrow ZN - CS^*PMS \tag{6}$$

$$ZN - CS^*PMS + Pollutants \rightarrow CO_2 + H_2O \tag{7}$$

3.4.2. Regeneration performance

In the recycling experiments, the removal of RhB was divided into two stages. To simplify the regeneration and reuse, we exclusively used deionized water to clean and dry the catalyst without taking special measures for the catalyst desorption. In the recycling experiments, the catalyst maintained the removal rate of over 90%

Fig. 7. The regeneration performance and reusability of the ZN-CS. Reaction conditions: $[RhB]_0^i = 7.60$ mg·L^{-1}, $[RhB]_0 = 3.40$ mg·L^{-1}, $[ZN-CS] = 100.00$ mg·L^{-1}, and $[PMS] = 200.00$ mg·L^{-1}.

as shown in Fig. 7. The regenerated catalyst exhibited better degradation effect on RhB. The reasons for the better recycling performance of the catalyst are as follows. First, the recycled samples exhibited a certain adsorption capacity towards RhB in the recycling experiments even without desorption. This was because some of the originally adsorbed RhB had been degraded in the batch experiments, and the recycled samples could recover a certain adsorption capacity. The second factor is that the generated free radicals or the ZN-CS*PMS mainly attacked the adsorbed dyes on the surface. The free RhB molecules in the solution were rarely attacked, resulting in a low decolorization rate in the solution during the degradation stage. In contrast, the pre-adsorption step was omitted in the recycling experiments, and the free radicals generated in the ZN-CS/PMS system attacked many free RhB molecules in the solution, thereby improving the removal efficiency. The third factor is that the main active sites in the adsorption and degradation stages were all surface hydroxyl groups. In the recycling experiments, only a fraction of the surface hydroxyl groups was occupied by the dye molecules, thereby leading to more available active sites and improved removal efficiency. This result indicated that the adsorption and degradation processes exhibited a coupling effect, and the ZN-CS maintained adequate performance in such a continuous process. The recyclability of the catalyst is conducive to promoting cleaner production techniques.

3.5. Mechanism of the coupling process

Based on the phenomenon and analysis mentioned above, we can summarize the mechanism of the entire process (Fig. 8). First, because of the van der Waals forces, electrostatic attraction, and hydrogen bond complexation, several RhB molecules were adsorbed on the catalyst surface leading to their partial removal from the solution. Simultaneously, the RhB molecules were transformed into two forms: the adsorbed form and the free form (free in the aqueous phase). After the addition of PMS, a radical and a non-radical pathway of the degradation were observed; these pathways simultaneously attacked the RhB molecules in both the forms. Subsequently, the free RhB in the solution was almost completely removed, and so was the adsorbed RhB. This resulted in the partial regeneration of the adsorption capacity of the ZN-CS. The catalyst was now ready for reuse. Furthermore, the surface hydroxyl groups were the main active sites for both the adsorption and degradation processes. Therefore, the degradation of the adsorbed RhB was conducive to the regeneration of the active sites that promotes the degradation process. This may be a reason for the improvement in the regeneration performance. Finally, the magnetic ZN-CS could be easily separated from the solution that had been degraded.

3.6. Removal of different organic compounds

To check the wide suitability of the ZN-CS, elimination experiments on different target contaminants (AO7, MB, Nor, and TC) were carried out using the ZN-CS/PMS system. Fig. 9 and Appendix A Fig. S11 illustrate the experimental results. The basic information about the target pollutants and experimental conditions are given in Table S5. MB is a typical cationic dye, AO7 is a typical anionic dye, and TC and Nor are representatives of pharmaceuticals and personal care products (PPCPs), respectively, in water. They exhibit different sizes and structures, different electronegativities in water, and different hydrogen bond receptors and donors, leading to their possibly different removal effects. As illustrated in Fig. 9, the ZN-CS/PMS system exhibits a removal efficiency of more than 70% for the AO7 removal, while in the PMS system, the removal effects could be ignored. The increase in the AO7 concentration in the solution phase at the fifth minute may be because of the addition
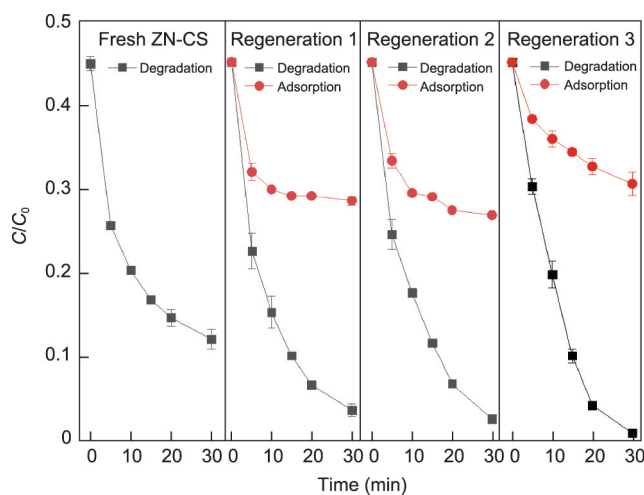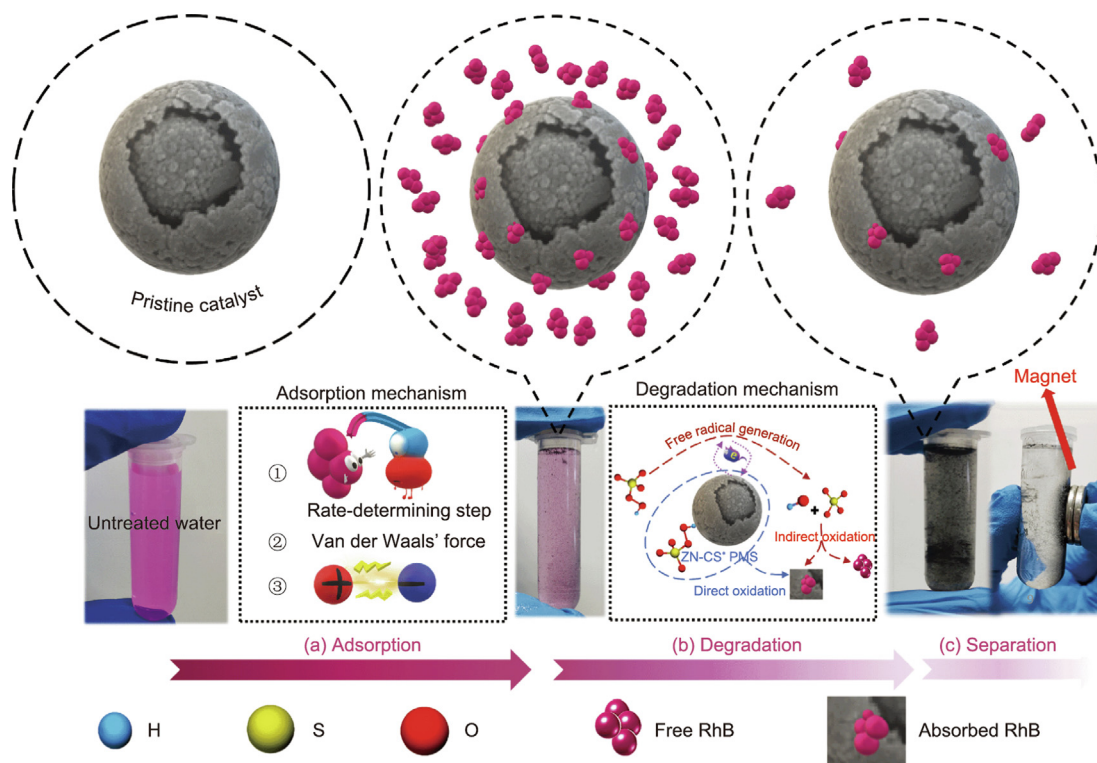
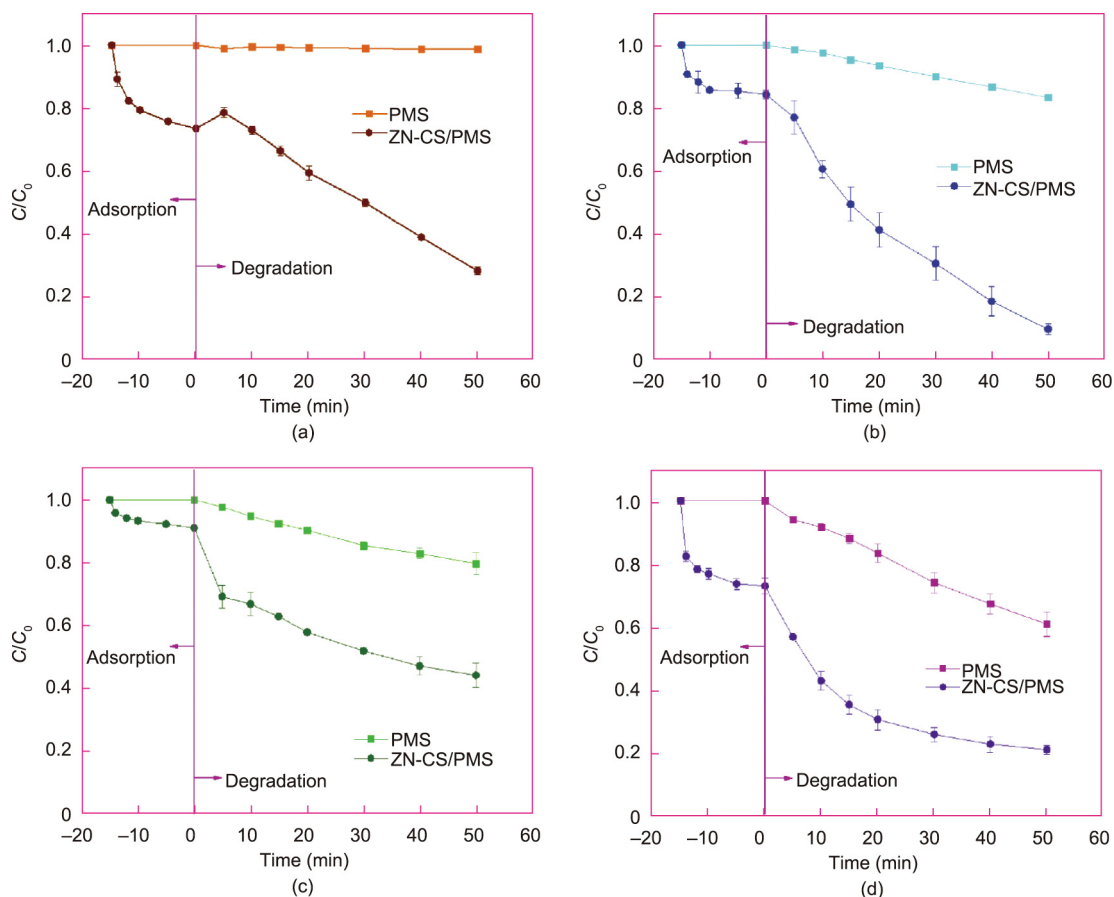**Fig. 8.** Possible mechanism of the coupling process. (a) Adsorption mechanism; (b) degradation mechanism; (c) separation.

Fig. 9. Different target contaminants absorbed and degraded by the ZN-CS/PMS system ([ZN-CS] = 100.00 mg·L^{-1}, [PMS] = 200.00 mg·L^{-1}, initial pH (pH$_{in}$) = pH$_0$): (a) AO7 (reaction condition: [AO7] = 10.00 mg·L^{-1}); (b) MB (reaction condition: [MB] = 4.00 mg·L^{-1}); (c) Nor (reaction condition: [Nor] = 5.00 mg·L^{-1}); and (d) TC (reaction condition: [TC] = 10.00 mg·L^{-1}).

of PMS that leads to the desorption of the partially adsorbed AO7. For MB, the ZN-CS/PMS system demonstrates over 90% removal efficiency, while the removal efficiency under the PMS system is less than 20%. For Nor, the system exhibits a removal efficiency of more than 50%, while the efficiency is approximately 20% in the PMS system. For TC, the removal efficiency of the system can reach approximately 80%, while the removal efficiency of the PMS system is approximately 40%. Appendix A Fig. S9 and Text S9 illustrate the effect of several vital parameters. Appendix A Fig. S12 illustrate the elimination of RhB in real water sample. In brief, the ZN-CS offers good adsorption and degradation efficiency towards various pollutants that exhibit different electric properties and sizes. Thus, the ZN-CS system presents a wide range of application prospects.

4. Conclusions

In summary, the magnetic composite ZnO/Ni$_3$ZnC$_{0.7}$ was successfully synthesized and developed as an effective adsorbent and a heterogeneous catalyst for the PMS oxidation to eliminate a variety of organic compounds. The magnetic properties of this nanocomposite led to a rapid and easy separation from the solutions. This study proposes a probable mechanism of the adsorption process that relates to the electrostatic factor and hydrogen bonding. The mechanism of the degradation process indicated that the organic compounds were mainly oxidized by the high-potential intermediate, ZN-CS*PMS, and the hydroxyl radicals generated by PMS, which were primarily activated by the surface hydroxyl groups. The adsorption capacity of the ZN-CS is regenerated owing to the maximum degradation of the adsorbed substrate, achieving the coupling effect. Compared with the systems used in some previous studies, this system used no precious metals. Moreover, this system employed the adsorption–degradation process to achieve a balance between the economic and treatment effect. Furthermore, the synthesized catalyst exhibits magnetic properties, recyclability, stable structure, and good removal efficiency for a variety of organic matter. Our work provides an insight into the development of highly efficient magnetic MOF-based materials for wastewater treatment, and has potential application prospects in the treatment of printing and dyeing wastewater or medical wastewater.

Compliance with ethical guidelines

Youwen Shuai, Xue Huang, Benyin Zhang, Lu Xiang, Hao Xu, Qian Ye, Jinfeng Lu, and Jing Zhang declare that they have no conflicts of interest or financial conflicts to disclose.

Appendix A. Supplementary data

Supplementary data to this article can be found online at https://doi.org/10.1016/j.eng.2021.08.029.

References

[1] Meyer MF, Powers SM, Hampton SE. An evidence synthesis of pharmaceuticals and personal care products (PPCPs) in the environment: imbalances among compounds, sewage treatment techniques, and ecosystem types. Environ Sci Technol 2019;53(22):12961–73.

[2] Isari AA, Hayati F, Kakavandi B, Rostami M, Motevassel M, Dehghanifard E. Cu co-doped TiO$_2$@functionalized SWCNT photocatalyst coupled with ultrasound and visible-light: an effective sono-photocatalysis process for pharmaceutical wastewaters treatment. Chem Eng J 2020;392:123685.

[3] Sumpter JP, Johnson AC. Lessons from endocrine disruption and their application to other issues concerning trace organics in the aquatic environment. Environ Sci Technol 2005;39(12):4321–32.

[4] Chu KH, Al-Hamadani YAJ, Park CM, Lee G, Jang M, Jang Am, et al. Ultrasonic treatment of endocrine disrupting compounds, pharmaceuticals, and personal care products in water: a review. Chem Eng J 2017;327:629–47.

[5] Bello MM, Abdul Raman AA, Purushothaman M. Applications of fluidized bed reactors in wastewater treatment-a review of the major design and operational parameters. J Clean Prod 2017;141:1492–514.

[6] Khan AH, Khan NA, Ahmed S, Dhingra A, Singh CP, Khan SU, et al. Application of advanced oxidation processes followed by different treatment technologies for hospital wastewater treatment. J Clean Prod 2020;269:122411.

[7] Luo Y, Guo W, Ngo HH, Nghiem LD, Hai FI, Zhang J, et al. A review on the occurrence of micropollutants in the aquatic environment and their fate and removal during wastewater treatment. Sci Total Environ 2014;473–474:619–41.

[8] Deng J, Feng SF, Zhang K, Li J, Wang H, Zhang T, et al. Heterogeneous activation of peroxymonosulfate using ordered mesoporous Co$_3$O$_4$ for the degradation of chloramphenicol at neutral pH. Chem Eng J 2017;308:505–15.

[9] Feng Y, Wu D, Deng Y, Zhang T, Shih K. Sulfate Radical-mediated degradation of sulfadiazine by CuFeO$_2$ rhombohedral crystal-catalyzed peroxymonosulfate: synergistic effects and mechanisms. Environ Sci Technol 2016;50(6):3119–27.

[10] Rezaei SS, Kakavandi B, Noorisepehr M, Isari AA, Zabih S, Bashardoust P. Photocatalytic oxidation of tetracycline by magnetic carbon-supported TiO$_2$ nanoparticles catalyzed peroxydisulfate: performance, synergy and reaction mechanism studies. Separ Purif Tech 2021;258:117936.

[11] Anipsitakis GP, Dionysiou DD. Radical generation by the interaction of transition metals with common oxidants. Environ Sci Technol 2004;38(13):3705–12.

[12] Ding D, Liu C, Ji Y, Yang Q, Chen L, Jiang C, et al. Mechanism insight of degradation of norfloxacin by magnetite nanoparticles activated persulfate: identification of radicals and degradation pathway. Chem Eng J 2017;308:330–9.

[13] Ghanbari F, Moradi M. Application of peroxymonosulfate and its activation methods for degradation of environmental organic pollutants. Chem Eng J 2017;310:41–62.

[14] Oh WD, Dong Z, Lim TT. Generation of sulfate radical through heterogeneous catalysis for organic contaminants removal: current development, challenges and prospects. Appl Catal B 2016;194:169–201.

[15] Babaei AA, Golshan M, Kakavandi B. A heterogeneous photocatalytic sulfate radical-based oxidation process for efficient degradation of 4-chlorophenol using TiO anchored on Fe oxides@carbon. Process Saf Environ Prot 2021;149:35–47.

[16] Rezaei SS, Dehghanifard E, Noorisepehr M, Ghadirinejad K, Kakavandi B, Esfahani AR. Efficient clean-up of waters contaminated with diazinon pesticide using photo-decomposition of peroxymonosulfate by ZnO decorated on a magnetic core/shell structure. J Environ Manage 2019;250:109472.

[17] Noorisepehr M, Ghadirinejad K, Kakavandi B, Ramazanpour Esfahani A, Asadi A. Photo-assisted catalytic degradation of acetaminophen using peroxymonosulfate decomposed by magnetic carbon heterojunction catalyst. Chemosphere 2019;232:140–51.

[18] Qiao J, Hamaya T, Okada T. Chemically modified poly(vinyl alcohol)-poly(2-acrylamido-2-methyl-1-propanesulfonic acid) as a novel proton-conducting fuel cell membrane. Chem Mater 2005;17(9):2413–21.

[19] Pirkanniemi K, Sillanpää M. Heterogeneous water phase catalysis as an environmental application: a review. Chemosphere 2002;48(10):1047–60.

[20] Wang X, Qin Y, Zhu L, Tang H. Nitrogen-doped reduced graphene oxide as a bifunctional material for removing bisphenols: synergistic effect between adsorption and catalysis. Environ Sci Technol 2015;49(11):6855–64.

[21] Peng Q, Ding Y, Zhu L, Zhang G, Tang H. Fast and complete degradation of norfloxacin by using Fe/Fe$_3$C@NG as a bifunctional catalyst for activating peroxymonosulfate. Separ Purif Tech 2018;202:307–17.

[22] Chen YZ, Zhang R, Jiao L, Jiang HL. Metal–organic framework-derived porous materials for catalysis. Coord Chem Rev 2018;362:1–23.

[23] Farrusseng D, Aguado S, Pinel C. Metal–organic frameworks: opportunities for catalysis. Angew Chem Int Ed Engl 2009;48(41):7502–13.

[24] James SL. Metal–organic frameworks. Chem Soc Rev 2003;32(5):276–88.

[25] Qasem NAA, Ben-Mansour R, Habib MA. An efficient CO$_2$ adsorptive storage using MOF-5 and MOF-177. Appl Energy 2018;210:317–26.

[26] Liu Y, Han G, Zhang X, Xing C, Du C, Cao H, et al. Co-Co$_3$O$_4$@carbon core−shells derived from metal−organic framework nanocrystals as efficient hydrogen evolution catalysts. Nano Res 2017;10(9):3035–48.

[27] Wang R, Xu H, Zhang Ke, Wei S, Deyong Wu. High-quality Al@Fe-MOF prepared using Fe-MOF as a micro-reactor to improve adsorption performance for selenite. J Hazard Mater 2019;364:272–80.

[28] Xu H, Gao J, Qian X, Wang J, He H, Cui Y, et al. Metal–organic framework nanosheets for fast-response and highly sensitive luminescent sensing of Fe^{3+}. J Mater Chem A Mater Energy Sustain 2016;4(28):10900–5.

[29] Teplensky MH, Fantham M, Li P, Wang TC, Mehta JP, Young LJ, et al. Temperature treatment of highly porous zirconium–containing metal–

organic frameworks extends drug delivery release. J Am Chem Soc 2017;139 (22):7522–32.

[30] Silva CG, Corma A, García H. Metal–organic frameworks as semiconductors. J Mater Chem 2010;20(16):3141–56.

[31] Keskin S, Kızılel S. Biomedical applications of metal organic frameworks. Ind Eng Chem Res 2011;50(4):1799–812.

[32] Cao X, Zheng B, Rui X, Shi W, Yan Q, Zhang H. Metal oxide-coated three-dimensional graphene prepared by the use of metal–organic frameworks as precursors. Angew Chem Int Ed Engl 2014;53(5):1404–9.

[33] Maya F, Palomino Cabello C, Frizzarin RM, Estela JM, Turnes Palomino G, Cerdà V. Magnetic solid-phase extraction using metal–organic frameworks (MOFs) and their derived carbons. TrAC Trends Analyt Chem 2017;90:142–52.

[34] Chen L, Li Y, Xu N, Zhang G. Metal–organic framework derived coralline-like non-precious metal catalyst for highly efficient oxygen reduction reaction. Carbon N Y 2018;132:172–80.

[35] Zhang H, Liu X, Wu Y, Guan C, Cheetham AK, Wang J. MOF-derived nanohybrids for electrocatalysis and energy storage: current status and perspectives. Chem Commun 2018;54(42):5268–88.

[36] Liu C, Wang Y, Zhang Y, Li R, Meng W, Song Z, et al. Enhancement of Fe@porous carbon to be an efficient mediator for peroxymonosulfate activation for oxidation of organic contaminants: incorporation NH₂-group into structure of its MOF precursor. Chem Eng J 2018;354:835–48.

[37] Li CX, Chen CB, Lu JY, Cui S, Li J, Liu HQ, et al. Metal organic framework-derived CoMn₂O₄ catalyst for heterogeneous activation of peroxymonosulfate and sulfanilamide degradation. Chem Eng J 2018;337:101–9.

[38] Hafizovic J, Bjørgen M, Olsbye U, Dietzel PDC, Bordiga S, Prestipino C, et al. The inconsistency in adsorption properties and powder XRD data of MOF-5 is rationalized by framework interpenetration and the presence of organic and inorganic species in the nanocavities. J Am Chem Soc 2007;129(12):3612–20.

[39] Qi ZP, Yang JM, Kang YS, Guo F, Sun WY. Facile water-stability evaluation of metal-organic frameworks and the property of selective removal of dyes from aqueous solution. Dalton Trans 2016;45(21):8753–9.

[40] Li H, Shi W, Zhao K, Li H, Bing Y, Cheng P. Enhanced hydrostability in Ni-doped MOF-5. Inorg Chem 2012;51(17):9200–7.

[41] Li J, Yan D, Hou S, Lu T, Yao Y, Chua DHC, et al. Metal–organic frameworks derived yolk-shell ZnO/NiO microspheres as high-performance anode materials for lithium-ion batteries. Chem Eng J 2018;335:579–89.

[42] Yang LY, Dong SY, Sun JH, Feng JL, Wu QH, Sun SP. Microwave-assisted preparation, characterization and photocatalytic properties of a dumbbell-shaped ZnO photocatalyst. J Hazard Mater 2010;179(1–3):438–43.

[43] Sarker M, Song JY, Jhung SH. Carboxylic-acid-functionalized UiO-66-NH₂: a promising adsorbent for both aqueous- and non-aqueous-phase adsorptions. Chem Eng J 2018;331:124–31.

[44] Pan B, Xing B. Adsorption mechanisms of organic chemicals on carbon nanotubes. Environ Sci Technol 2008;42(24):9005–13.

[45] Ghorai S, Sarkar A, Raoufi M, Panda AB, Schönherr H, Pal S. Enhanced removal of methylene blue and methyl violet dyes from aqueous solution using a nanocomposite of hydrolyzed polyacrylamide grafted xanthan gum and incorporated nanosilica. ACS Appl Mater Interfaces 2014;6(7):4766–77.

[46] Sing KSW, Everett DH, Haul RAW, Moscou L, Pierotti RA, Rouquerol J, et al. Reporting physisorption data for gas/solid systems with special reference to the determination of surface area and porosity. Pure Appl Chem 1985;57 (4):603–19.

[47] Liu M, Xu J, Cheng B, Ho W, Yu J. Synthesis and adsorption performance of Mg (OH)₂ hexagonal nanosheet-graphene oxide composites. Appl Surf Sci 2015;332:121–9.

[48] Kasnavia T, Vu D, Sabatini DA. Fluorescent dye and media properties affecting sorption and tracer selection. Ground Water 1999;37(3):376–81.

[49] Zhang T, Li W, Croué JP. Catalytic ozonation of oxalate with a cerium supported palladium oxide: an efficient degradation not relying on hydroxyl radical oxidation. Environ Sci Technol 2011;45(21):9339–46.

[50] Liu J, Zhao Z, Shao P, Cui F. Activation of peroxymonosulfate with magnetic Fe₃O₄–MnO₂ core–shell nanocomposites for 4-chlorophenol degradation. Chem Eng J 2015;262:854–61.

[51] Mo X, Yang ZH, Xu HY, Zeng GM, Huang J, Yang X, et al. Combination of cathodic reduction with adsorption for accelerated removal of Cr(VI) through reticulated vitreous carbon electrodes modified with sulfuric acid-glycine co-doped polyaniline. J Hazard Mater 2015;286:493–502.

[52] Wang L, Li J, Wang Z, Zhao L, Jiang Q. Low-temperature hydrothermal synthesis of α-Fe/Fe₃O₄ nanocomposite for fast Congo red removal. Dalton Trans 2013;42(7):2572–9.

[53] Zhang T, Li C, Ma J, Tian H, Qiang Z. Surface hydroxyl groups of synthetic α-FeOOH in promoting ·OH generation from aqueous ozone: property and activity relationship. Appl Catal B 2008;82(1-2):131–7.

[54] Lu Y, Jiang B, Fang L, Ling F, Gao J, Wu F, et al. High performance NiFe layered double hydroxide for methyl orange dye and Cr(VI) adsorption. Chemosphere 2016;152:415–22.

[55] Lei C, Zhu X, Le Y, Zhu B, Yu J, Ho W. Hierarchically porous NiO–Al₂O₃ nanocomposite with enhanced Congo red adsorption in water. RSC Adv 2016;6 (13):10272–9.

[56] Ho YS, McKay G. Pseudo-second order model for sorption processes. Process Biochem 1999;34(5):451–65.

[57] Neta P, Huie RE, Ross AB. Rate constants for reactions of inorganic radicals in aqueous solution. J Phys Chem Ref Data 1988;17(3):1027–284.

[58] Buxton GV, Greenstock CL, Helman WP, Ross AB. Critical review of rate constants for reactions of hydrated electrons, hydrogen atoms and hydroxyl radicals (·OH/·O⁻) in aqueous solution. J Phys Chem Ref Data 1988;17(2):513.

[59] Hayon E, Treinin A, Wilf J. Electronic spectra, photochemistry, and autoxidation mechanism of the sulfite–bisulfite–pyrosulfite systems. The SO₂⁻, SO₃⁻, SO₄⁻, and SO₅⁻ radicals. J Am Chem Soc 1972;94(1):47–57.

[60] Huang GX, Wang CY, Yang CW, Guo PC, Yu HQ. Degradation of bisphenol a by peroxymonosulfate catalytically activated with Mn₁.₈Fe₁.₂O₄ nanospheres: synergism between Mn and Fe. Environ Sci Technol 2017;51(21):12611–8.

[61] Feng M, Qu R, Zhang X, Sun P, Sui Y, Wang L, et al. Degradation of flumequine in aqueous solution by persulfate activated with common methods and polyhydroquinone-coated magnetite/multi-walled carbon nanotubes catalysts. Water Res 2015;85:1–10.

[62] Zhong H, Brusseau ML, Wang Y, Yan N, Quig L, Johnson GR. In-situ activation of persulfate by iron filings and degradation of 1,4-dioxane. Water Res 2015;83:104–11.

[63] Yan N, Liu F, Xue Q, Brusseau ML, Liu Y, Wang J. Degradation of trichloroethene by siderite-catalyzed hydrogen peroxide and persulfate: investigation of reaction mechanisms and degradation products. Chem Eng J 2015;274:61–8.

[64] Evans DF, Upton MW. Studies on singlet oxygen in aqueous solution. Part 3. The decomposition of peroxy-acids. J Chem Soc Dalton Trans 1985 (6):1151.

[65] Shao P, Tian J, Yang F, Duan X, Gao S, Shi W, et al. Identification and regulation of active sites on nanodiamonds: establishing a highly efficient catalytic system for oxidation of organic contaminants. Adv Funct Mater 2018;28 (13):1705295.

[66] Anipsitakis GP, Dionysiou DD. Degradation of organic contaminants in water with sulfate radicals generated by the conjunction of peroxymonosulfate with cobalt. Environ Sci Technol 2003;37(20):4790–7.

[67] Liang P, Zhang C, Duan X, Sun H, Liu S, Tade MO, et al. An insight into metal organic framework derived N-doped graphene for the oxidative degradation of persistent contaminants: formation mechanism and generation of singlet oxygen from peroxymonosulfate. Environ Sci Nano 2017;4(2):315–24.

[68] Montgomery RE. Catalysis of peroxymonosulfate reactions by ketones. J Am Chem Soc 1974;96(25):7820–1.

[69] Sun H, Feng X, Wang S, Ang HM, Tadé MO. Combination of adsorption, photochemical and photocatalytic degradation of phenol solution over supported zinc oxide: effects of support and sulphate oxidant. Chem Eng J 2011;170(1):270–7.

[70] Ramachandran R, Sakthivel T, Li M, Shan H, Xu ZX, Wang F. Efficient degradation of organic dye using Ni-MOF derived NiCo-LDH as peroxymonosulfate activator. Chemosphere 2021;271:128509.

[71] Zhu J, Chen C, Li Y, Zhou L, Lan Y. Rapid degradation of aniline by peroxydisulfate activated with copper–nickel binary oxysulfide. Separ Purif Tech 2019;209:1007–15.

[72] Ding Y, Wang X, Fu L, Peng X, Pan C, Mao Q, et al. Nonradicals induced degradation of organic pollutants by peroxydisulfate (PDS) and peroxymonosulfate (PMS): recent advances and perspective. Sci Total Environ 2021;765:142794.

[73] Ren W, Xiong L, Nie G, Zhang H, Duan X, Wang S. Insights into the electron-transfer regime of peroxydisulfate activation on carbon nanotubes: the role of oxygen functional groups. Environ Sci Technol 2020;54(2):1267–75.

[74] Kleinwechter H, Janzen C, Knipping J, Wiggers H, Roth P. Formation and properties of ZnO nano-particles from gas phase synthesis processes. J Mater Sci 2002;37(20):4349–60.

[75] Aljawfi RN, Mollah S. Properties of Co/Ni codoped ZnO based nanocrystalline DMS. J Magn Magn Mater 2011;323(23):3126–32.

[76] Cun T, Dong C, Huang Q. Ionothermal precipitation of highly dispersive ZnO nanoparticles with improved photocatalytic performance. Appl Surf Sci 2016;384:73–82.

[77] Lei C, Pi M, Jiang C, Cheng B, Yu J. Synthesis of hierarchical porous zinc oxide (ZnO) microspheres with highly efficient adsorption of Congo red. J Colloid Interface Sci 2017;490:242–51.

[78] Luo H, Lin Q, Zhang X, Huang Z, Fu H, Xiao R, et al. Determining the key factors of nonradical pathway in activation of persulfate by metal-biochar nanocomposites for bisphenol A degradation. Chem Eng J 2020;391:123555.

[79] Hong XJ, Song CL, Wu ZM, Li ZH, Cai YP, Wang CX, et al. Sulfophilic and lithophilic sites in bimetal nickel–zinc carbide with fast conversion of polysulfides for high-rate Li–S battery. Chem Eng J 2021;404:126566.